

CONSTRAINING COSMOLOGICAL PARAMETERS USING THE CLUSTER MASS-RICHNESS RELATION

MOHAMED H. ABDULLAH^{1,2}, GILLIAN WILSON³, ANATOLY KLYPIN^{4,5}, AND TOMOAKI ISHIYAMA¹

¹Institute of Management and Information Technologies, Chiba University, 1-33, Yayoi-cho, Inage-ku, Chiba, 263-8522, Japan

²Department of Astronomy, National Research Institute of Astronomy and Geophysics, Cairo, 11421, Egypt

³Department of Physics and Astronomy, University of California Riverside, 900 University Avenue, Riverside, CA 92521, USA

⁴Astronomy Department, New Mexico State University, Las Cruces, NM 88001 and

⁵Department of Astronomy, University of Virginia, Charlottesville, VA 22904, USA

Draft version October 19, 2022

ABSTRACT

The cluster mass-richness relation (MRR) is an observationally efficient and potentially powerful cosmological tool for constraining the mean matter density of the universe Ω_m and the amplitude of fluctuations σ_8 using the cluster abundance technique. We derive the MRR relation using *GalWCat19*, a publicly available galaxy cluster catalog we created from the Sloan Digital Sky Survey-DR13 spectroscopic dataset. The MRR shows a tail at the low-richness end. Using the Illustris-TNG and mini-Uchuu cosmological numerical simulations, we demonstrate that this tail is caused by systematic uncertainties. We show that, by means of a judicious cut, identified by the use of the Hinge function, it is possible to determine a richness threshold above which the MRR is linear i.e., where cluster mass scales with richness as $\log M_{200} = \alpha + \beta \log N_{200}$. We derive the MRR and show it is consistent with both sets of simulations with a slope of $\beta \approx 1$. We use our MRR to estimate cluster masses from the *GalWCat19* catalog which we then use to set constraints on Ω_m and σ_8 . Utilizing the all-member MRR, we obtain constraints of $\Omega_m = 0.31^{+0.04}_{-0.03}$ and $\sigma_8 = 0.82^{+0.05}_{-0.04}$, and utilizing the red-member MRR, we obtain $\Omega_m = 0.31^{+0.04}_{-0.03}$ and $\sigma_8 = 0.81^{+0.05}_{-0.04}$. Our constraints on Ω_m and σ_8 are consistent and very competitive with the *Planck 2018* results.

Keywords: galaxies: clusters: general - cosmology - cosmological parameters

1. INTRODUCTION

In the current picture of structure formation, galaxy clusters arise from rare high peaks of the initial density fluctuation field. These peaks grow in a hierarchical fashion through the dissipationless mechanism of gravitational instability with more massive halos growing via continued accretion and merging of low-mass halos (White & Frenk 1991; Kauffmann et al. 1999, 2003). Galaxy clusters are the most massive virialized systems in the universe and are amongst the most effective probes of cosmology. An accurate measurement of the cluster abundance can be used to determine cosmological parameters. The cluster mass function (CMF¹), or the abundance of galaxy clusters, is particularly sensitive to two cosmological parameters in particular, Ω_m , the matter density of the universe and σ_8 , the rms mass fluctuation on the scale of $8 h^{-1}$ Mpc at $z = 0$ (e.g., Wang & Steinhardt 1998; Battye & Weller 2003; Dahle 2006; Wen et al. 2010).

One of the biggest limitations to utilizing the cluster abundance as a cosmological tool is the difficulty of obtaining an accurate estimate of cluster masses because cluster mass is not a directly observable quantity. It can be estimated indirectly using different methods, such as, the virial mass estimator (e.g., Binney & Tremaine 1987), weak gravitational lensing (e.g., Wilson et al. 1996; Holhjem et al. 2009), or application of the Jeans equation of the gas density calculated from the X-ray analysis of a

galaxy cluster (e.g., Sarazin 1988). However, these methods are observationally expensive, require high-quality data sets, and are biased owing to the assumptions that have to be made (e.g., spherical symmetry, hydrostatic equilibrium, and galaxies as tracers of the underlying mass distribution). Fortunately, the cluster mass can still be indirectly inferred from other observables, the so called mass proxies, which scale tightly with cluster mass. Among these mass proxies are X-ray luminosity, temperature, the product of X-ray temperature and gas mass (e.g., Pratt et al. 2009; Vikhlinin et al. 2009; Mantz et al. 2016), optical luminosity (e.g., Yee & Ellingson 2003), and the velocity dispersion of member galaxies (e.g., Biviano et al. 2006; Bocquet et al. 2015). In particular, cluster richness (total number of member galaxies with luminosities larger than a certain luminosity threshold) is extensively used in the literature (e.g., Pereira et al. 2018; DES Collaboration et al. 2020) as a mass calibration, and commonly referred to as the mass-richness relation (hereafter MRR).

Another challenge arises because of the well-known degeneracy between Ω_m and σ_8 : the fact that it is possible to obtain a similar cluster abundance from a variety of different combinations of values of Ω_m and σ_8 . Figure 1 illustrates this degeneracy. It shows the effect on the cluster abundance of fixing each of the two parameters in turn, while varying the other. Using the functional form of the halo mass function provided by Tinker et al. (2008) we calculate the HMF and then plot the expected number and masses of clusters within a fixed volume. As shown in Figure 1, increasing Ω_m while fixing σ_8 results in increased numbers of clusters of all masses. Interestingly, increasing σ_8 while fixing Ω_m also results in increased

melha004@ucr.edu

¹ Throughout the paper we use CMF for mass functions derived from observations and HMF for mass functions computed by theoretical models.

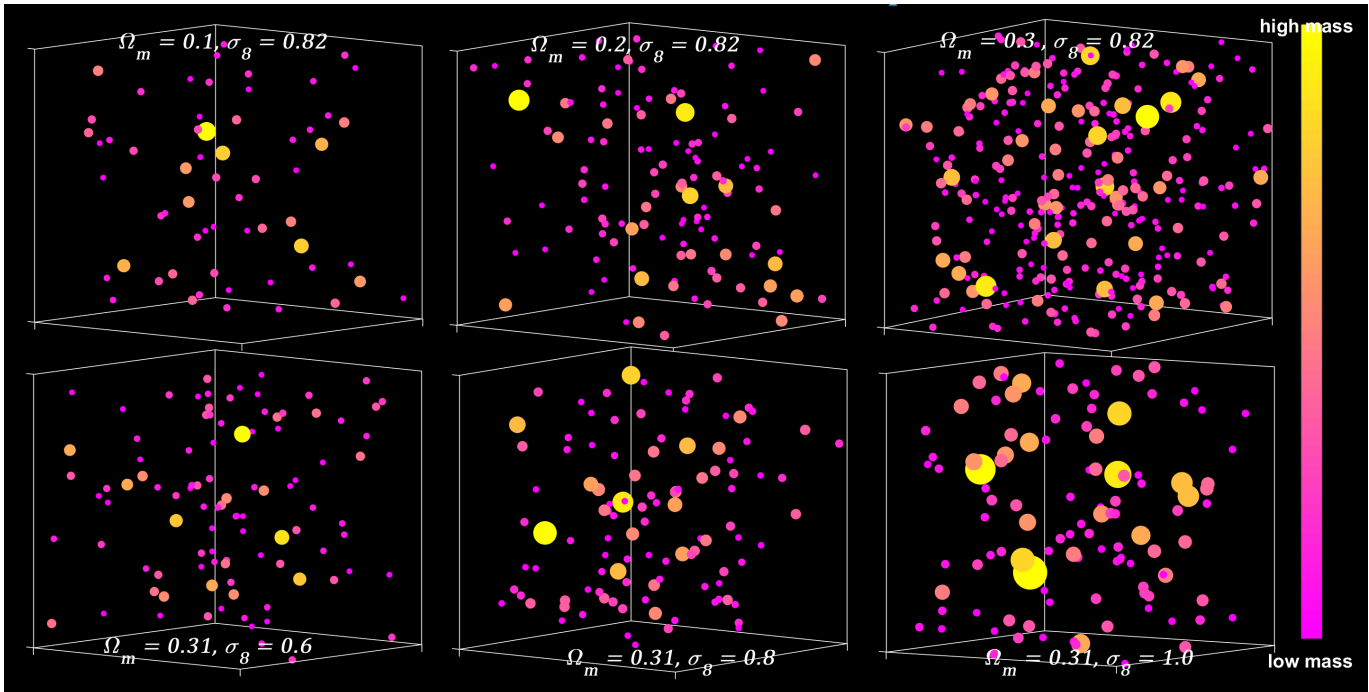


Figure 1. Schematic diagram showing the effect on the number of clusters and their masses of varying Ω_m (upper) and σ_8 (lower) independently while holding the other parameter fixed. Each circle represents a cluster with its size (large to small) and color (yellow to magenta) indicating high to low mass. A larger value of Ω_m results in an approximately proportionally higher number of clusters of every mass. A larger value of σ_8 also results in a higher number of clusters of every mass but also changes the ratio of high to low mass clusters, so results in a larger number of high mass clusters relative to low mass clusters. Note that the clusters are distributed randomly in each box.

numbers of clusters of all masses. However, increasing σ_8 increases the number of high-mass clusters more dramatically than the number of low-mass clusters. In other words, σ_8 is very sensitive to the high-mass end of the HMF. Large wide deep-field imaging and spectroscopic galaxy surveys observing over a range of redshift, such as DES (Abbott et al. 2018), DESI (Levi et al. 2019), Euclid (Euclid Collaboration et al. 2019), eROSITA (Merloni et al. 2012), the LSST that be carried out at the Vera C. Rubin Observatory (LSST Science Collaboration et al. 2009), the High Latitude Wide Area Survey that will be carried out at the Nancy Grace Roman Telescope (Akeson et al. 2019), SPHEREX (Doré et al. 2014), and the Subaru Prime Focus Spectrograph (PFS) (Takada et al. 2014) will collectively and simultaneously increase the precision of the constraints on Ω_m and σ_8 , break the degeneracy between them, and also constrain additional parameters such as the dark energy Ω_Λ , and the equation of state ω (e.g., Rozo et al. 2010; Weinberg et al. 2013; Planck Collaboration et al. 2018).

The MRR is an observationally cheap but potentially powerful cosmological tool. With a deluge of deep, wide-area multi-passband imaging becoming available from a slew of ground and space surveys, there is renewed interest in exploring the potential of the MRR for constraining cosmological parameters. Masses of individual galaxy clusters can be estimated using the MRR relation, and then used to derive the CMF and constrain Ω_m and σ_8 . This cluster abundance technique using cluster masses derived from the MRR (CA_{MRR} ; see Table 1) has traditionally been applied to photometric galaxy cluster catalogs which lack estimates of individual cluster masses e.g. Rozo et al. 2010; Costanzi et al. 2019; Kirby et al.

2019; Lesci et al. 2022.

Cluster catalogs constructed from photometric surveys provide optical richnesses for a very large number of groups and clusters, but may introduce large systematics. This is because distances inferred from photometric redshift estimates are less accurate than those inferred from spectroscopic redshifts. This increases the incidence of line-of-sight galaxies in close projection which are falsely-assigned as cluster members. Moreover, cluster catalogs constructed from photometric surveys do not return an estimate of each cluster’s mass. For such photometric samples the cluster mass must be inferred indirectly from the optical richness, which scales tightly with cluster mass. To estimate cluster masses for these photometric samples it is necessary to follow up a subset of clusters with known masses which are calculated individually using different mass estimators such as weak lensing or X-ray observations. Cluster masses can also be estimated using stacked weak lensing mass profiles by calculating the mean mass of the clusters in a richness bin (e.g., Simet et al. 2017). Then, the MRR can be calibrated for these samples. As a result of these challenges (as we discuss further below), the MRRs derived from previous studies (e.g., Johnston et al. 2007; Wiesner et al. 2015; Melchior et al. 2017) are in tension with each other, even in the case of studies which use the same type of cluster sample. This is the main reason for the discrepancies or tensions among the derived cosmological parameters (see Abdullah et al. 2020a).

To better understand how to apply the MRR in the absence of spectroscopy (spectroscopy sparse), we analyze a photometric cluster catalog for which spectroscopy exists. Specifically, we derive the MRR, the average mass

for a cluster that has N galaxies, using the spectroscopic GalWCat19 cluster catalog. Then we pretend that we do not know the true cluster mass and use MRR to find it. This procedure tests the scatter in MRR and potential systematics.

The GalWCat19 catalog is in the redshift range of $0.01 \leq z_{cl} \leq 0.2$ with masses $M_{200} \geq 0.4 \times 10^{14} h^{-1} M_{\odot}$ (Abdullah et al. 2020b). The advantages of using the GalWCat19 catalog are as follow. The GalWCat19 was derived from the Sloan Digital Sky Survey-Data Release 13 spectroscopic dataset (hereafter SDSS DR13², Albareti et al. 2017). The clusters were first identified by looking for the Finger-of-God effect (see, Jackson 1972; Kaiser 1987; Abdullah et al. 2013). The cluster membership was constructed by applying the GalWeight technique which was specifically designed to simultaneously maximize the number of *bona fide* cluster members while minimizing the number of contaminating interlopers (Abdullah et al. 2018). The cluster masses were calculated individually from the dynamics of the member galaxies via the virial theorem (e.g., Limber & Mathews 1960; Abdullah et al. 2011), and corrected for the surface pressure term (e.g., The & White 1986; Carlberg et al. 1997). A main advantage of our approach is that it returns an estimate of the total cluster mass without making any assumptions about the internal complicated physical processes associated with the baryons (gas and stars).

In the first part of the paper we derive the relationship between the dynamical mass and the optical richness. Note that we derive the MRR relations for: (i) all members within R_{200} ³ (hereafter MRR_{all}) and (ii) for the red-only members within R_{200} (hereafter MRR_{red}). Notice that red galaxies are identified using red-sequence region in the color-magnitude diagram (e.g., Hao et al. 2009, see Appendix A1). In the second part of the paper, we utilize the MRR to estimate cluster masses and then to derive the cosmological parameters. For this purpose, we assume that the GalWCat19 catalog provides only the richness of each cluster, but we do not use cluster mass given by the catalog. Instead, we apply the derived MRR relations to estimate the cluster masses. We then construct cluster mass function and derive the cosmological parameters of Ω_m and σ_8 .

The paper is organized as follows. In § 2, we briefly describe the GalWCat19 cluster catalog, which we use in deriving the MRR. We discuss how we determine the completeness of the catalog as a function of mass and redshift, and how we determine the richness of each cluster. In § 3, we describe the basic ingredients and methodology of the MRR analysis and our results of the MRR parameters. In § 4, we present our constraint on the cosmological parameters of Ω_m and σ_8 for the GalWCat19 cluster catalog and compare our results with the previous studies. We summarize our conclusions and future work in § 5. Throughout the paper we adopt Λ CDM with

² <https://www.sdss.org/dr13/>

³ Throughout the paper we assume R_{200} is the virial radius of the cluster and M_{200} is the virial mass enclosed within R_{200} . In practice, the virial radius at which the cluster is in hydrostatic equilibrium cannot be determined. We follow convention and assume that the virial radius R_{200} is the radius within which the average density $\langle \rho(r < R_{200}) \rangle = 200\rho_c$, where ρ_c is the critical density of the universe.

$\Omega_m = 1 - \Omega_{\Lambda}$, and $H_0 = 100 h \text{ km s}^{-1} \text{ Mpc}^{-1}$. Note that throughout the paper we assume \log for \log_{10} .

2. DATA

2.1. The GalWCat19 Cluster Catalog

In this section we summarize how the GalWCat19 cluster catalog was created. Full details can be found in Abdullah et al. (2020b). Using both the photometric and spectroscopic datasets from SDSS-DR13, we extract data for all galaxies that satisfy the following set of criteria: spectroscopic detection, photometric and spectroscopic classification as galaxy (by the automatic pipeline), spectroscopic redshift between 0.001 and 0.2 (with a redshift completeness > 0.7 , Yang et al. 2007; Tempel et al. 2014), r-band magnitude (reddening-corrected) < 18 , flag SpecObj.zWarning = zero (indicating a well-measured redshift). This results in a catalog containing 704,200 galaxies satisfying all of the criteria.

Galaxy clusters were identified by the well-known Finger-of-God effect (FoG, Jackson 1972; Kaiser 1987; Abdullah et al. 2013). We applied the binary tree algorithm (e.g., Serra et al. 2011) to accurately determine the cluster center and a phase-space diagram. Galaxy membership for each cluster was assigned by applying the GalWeight technique (developed by our group and presented in Abdullah et al. (2018)) to galaxies in the phase-space diagram out to a maximum projected radius of $10 h^{-1} \text{ Mpc}$ and within a maximum line-of-sight velocity range of $\pm 3000 \text{ km s}^{-1}$. In Abdullah et al. (2018), using the Bolshoi simulation (Klypin et al. 2016), we showed that GalWeight was $\sim 98\%$ accurate in assigning cluster membership for clusters with mass $M_{200} > 2 \times 10^{14} h^{-1} M_{\odot}$ and $\sim 85\%$ for clusters with mass $M_{200} > 0.4 \times 10^{14} h^{-1} M_{\odot}$.

After applying GalWeight to determine cluster membership, the virial mass of each cluster was estimated. This was done by applying the virial theorem under the assumption that the mass distribution follows the galaxy distribution (e.g., Giuricin et al. 1982; Merritt 1988). The estimated mass was then corrected for the surface pressure term which, otherwise, would overestimate the true cluster mass (e.g., The & White 1986; Binney & Tremaine 1987). The cluster virial mass was calculated at the virial radius within which the cluster is in hydrostatic equilibrium. The virial radius is approximately equal to the radius within which the density $\rho = \Delta_{200}\rho_c$, where ρ_c is the critical density of the universe and $\Delta_{200} = 200$ (e.g., Carlberg et al. 1997; Klypin et al. 2016). Abdullah et al. (2020b) showed that the cluster mass estimates returned by the virial theorem performed very favorably, when compared to other commonly utilized mass estimation techniques, which were described and compared in Old et al. 2015.

The GalWCat19 catalog is publicly available from the website <http://cdsarc.u-strasbg.fr/viz-bin/cat/J/ApJS/246/2>. As described in Abdullah et al. (2020b), it consists of two tables, one characterizing the clusters and another characterizing the member galaxies. In creating the GalWCat19 catalog, a Λ CDM cosmology with $\Omega_m = 1 - \Omega_{\Lambda}$, and $H_0 = 100 h \text{ km s}^{-1} \text{ Mpc}^{-1}$ was assumed. The list of clusters has 1800 clusters with redshifts in the range $0.01 < z < 0.2$ and total masses in the range $(0.4 - 14) \times 10^{14} h^{-1} M_{\odot}$. The cluster table

Table 1
List of abbreviations used in this paper.

Abbreviation	Definition
MRR	mass-richness relation
MRR _{all}	mass-richness relation derived for all member galaxies within R_{200}
MRR _{red}	mass-richness relation derived for red member galaxies within R_{200}
α	normalization of the mass-richness relation
β	slope of the mass-richness relation
σ_{int}	intrinsic scatter in the mass-richness relation
N_{th}	richness threshold
\mathcal{S}_{fid}	a fiducial subsample of 756 clusters with $\log M_{200} \geq 13.9 [h^{-1} M_{\odot}]$ and $0.045 \leq z \leq 0.125$
$\mathcal{S}_{\text{all}17}$	a fiducial subsample of clusters with $\log M_{200} \geq 13.9 [h^{-1} M_{\odot}]$, $0.045 \leq z \leq 0.125$ and $N_{\text{th}} = 17$ for all members within R_{200}
$\mathcal{S}_{\text{red}13}$	a fiducial subsample of clusters with $\log M_{200} \geq 13.9 [h^{-1} M_{\odot}]$, $0.045 \leq z \leq 0.125$ and $N_{\text{th}} = 13$ for red members within R_{200}
f_x	fractional scatter defined as $f_x = (x - x_{\text{fid}})/x_{\text{fid}}$, and x , and x_{fid} are the estimated and fiducial parameters
MCMC	Markov chain Monte Carlo
CMF	cluster mass function
HMF	halo mass function
CA _{MRR}	deriving constraints on Ω_m and σ_8 using the cluster abundance technique and cluster mass estimates from the mass-richness relation
CA _{dyn}	deriving constraints on Ω_m and σ_8 using the cluster abundance technique and cluster mass estimates from the dynamics of member galaxies
CMB	deriving constraints on Ω_m and σ_8 using the cosmic microwave background radiation (CMB) technique

also contains the coordinates of each cluster on the sky (RA, Dec), redshift, number of members, velocity dispersion, and dynamical mass within four overdensities ($\Delta = 500, 200, 100, 5.5$). Note that merging clusters have been removed. The GalWCat19 galaxy member table contains 34,471 members which were identified to lie within the virial radius at which the density is 200 times the critical density of the Universe. The galaxy table contains the coordinates of each member galaxy and the ID of the host cluster.

In the remainder of this paper, we will be primarily focused on analyzing the GalWCat19 cluster table and will utilize the GalWCat19 galaxy member table only to calculate the richness of each cluster (see § 3). For brevity, therefore, hereafter when we refer to the GalWCat19 catalog, we are referring to the GalWCat19 cluster table.

2.2. Completeness

Abdullah et al. (2020a) showed that GalWCat19 is incomplete in redshift at $z > 0.085$ but that it was possible to correct for this incompleteness in redshift if each cluster at $z > 0.085$ was weighted by a selection function given by

$$\mathcal{S}_z(D) = 1.07 \exp \left[- \left(\frac{D}{293.4} \right)^{2.97} \right], \quad (1)$$

where D is the comoving distance to the cluster, and with the condition that $\mathcal{S}_z \leq 1$. Thus, the weight which is applied to any given cluster at redshift z is $\mathcal{W}_z = 1/\mathcal{S}_z(D)$. Caution is advised in using \mathcal{S}_z to weight those clusters which are at higher redshift in the GalWCat19 catalog. This is because above a redshift threshold, the weight becomes disproportionately large and introduces a high scatter and bias in the CMF toward the highest redshift clusters in the catalog. Thus, in order to avoid these effects we restrict our sample to a maximum redshift of $z = 0.125$.

Abdullah et al. (2020a) also showed that the value of mass at which the catalog is complete depends slightly on the cosmology, but that GalWCat19 is approximately complete for clusters with masses of $\log(M) \geq 13.9 h^{-1} M_{\odot}$. If we apply the above redshift incompleteness

correction and restrict our sample to clusters with redshifts of $0.045 \leq z \leq 0.125$ and masses of $\log(M) \geq 13.9 h^{-1} M_{\odot}$, a total of 756 clusters remain ($\approx 42\%$ of the GalWCat19 sample). We call this fiducial subsample of clusters, \mathcal{S}_{fid} . In § 4.3, we discuss the systematics introduced by adopting these redshift and mass thresholds on our best-fit estimates of Ω_m and σ_8 .

2.3. Richness

In this section we discuss how we calculate the richness of each cluster. For each cluster member, we calculate the absolute magnitude in the r -band, M_r , using

$$M_r - 5 \log h = m_r - DM - K(z) - E(z) \quad (2)$$

where $DM(z) = 5 \log D_L - 5 \log h - 25$ is the distance modulus calculated from the luminosity distance D_L , M_r is the AB apparent magnitude in the r -band converted from the SDSS magnitude as $m_{AB} = m_{sdss} + 0.010$, $K(z)$ is the K -correction, calculated using the latest version of “Kcorrect” (v4), and $E = Q(z - 0.1)$ with $Q = -1.62$ is the evolutionary correction in the r -band (see Blanton et al. 2003; Blanton & Roweis 2007 for details). Absolute magnitudes are $K(z)$ - and $E(z)$ -corrected to redshift $z = 0.1$, which is approximately equal to the mean redshift of the GalWCat19 catalog ($Z = 0.089$).

We define the richness of each cluster, N_{200} , as the total number of members within R_{200} and luminosities $L \geq 0.4L^*$. L^* is the evolved characteristic luminosity of galaxies in the r band defined as $L^*(z) = L^*(z = 0.1)10^{Q(z-0.1)}$ and $L^*(z = 0.1)$ is equivalent to a characteristic absolute magnitude $M_r^* = -20.44$ in the r band (Blanton et al. 2003). This is equivalent to a stellar mass of $\sim 5 \times 10^9 h^{-1} M_{\odot}$ (Deason et al. 2019).

While the GalWeight technique has been shown to be effective at removing foreground/background galaxies (Abdullah et al. 2018), some interlopers which are embedded in the cluster field due to the triple-value problem (see Tonry & Davis 1981; Abdullah et al. 2020b) still remain in the GalWCat19 catalog and these need to be removed before the MRR can be constructed. As discussed in Abdullah et al. (2018), the percentage of these interlopers is about 11%. The total number of galaxies

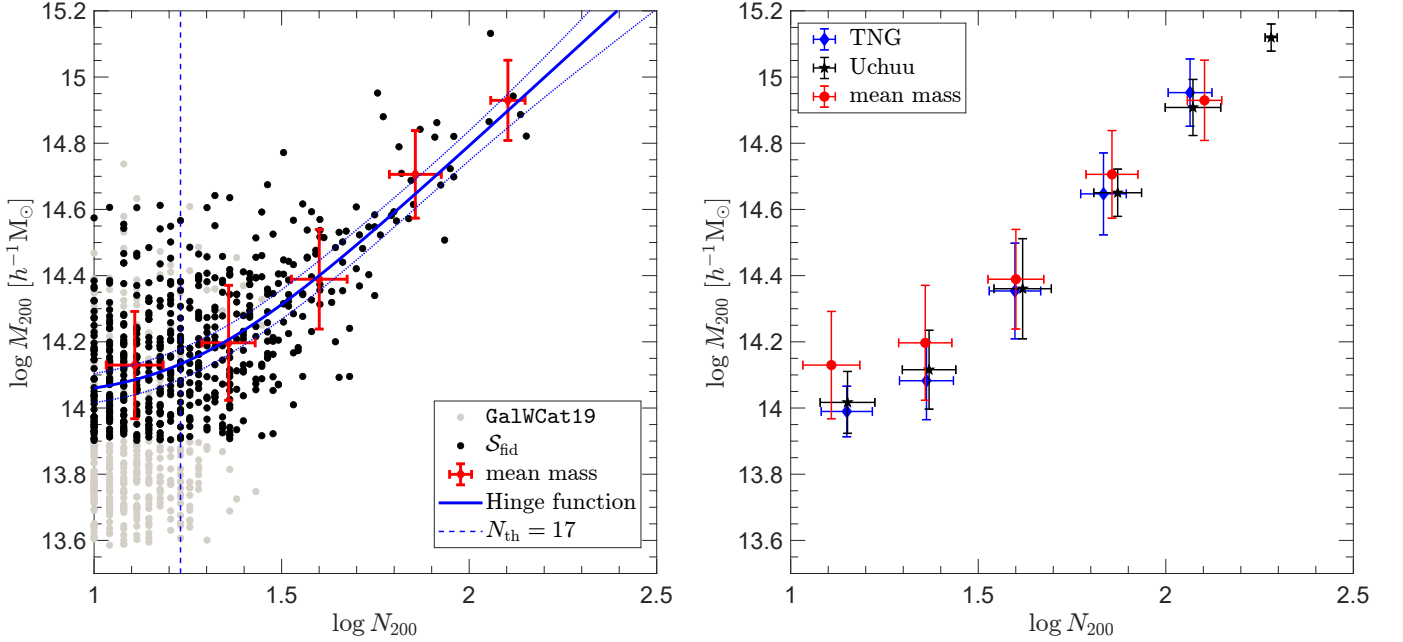


Figure 2. Left: Distribution of clusters from the GalWCat19 catalog in the mass-richness plane. Gray points show all 1800 clusters (with masses of $\log M_{200} \geq 13.5 h^{-1} M_{\odot}$ and at a redshift $z < 0.2$ (see § 2.3)). Black points show the complete fiducial (\mathcal{S}_{fid}) subsample of 756 clusters to which the redshift selection function has been applied ($\log M_{200} \geq 13.9 h^{-1} M_{\odot}$ and $0.045 \leq z \leq 0.125$; see § 3.2). The mean mass of clusters in \mathcal{S}_{fid} as a function of their richness are shown as solid red circles, with error bars indicating 1σ Poisson uncertainties. The blue solid line shows the Hinge function for \mathcal{S}_{fid} (see § 2.5), with the dotted blue lines indicating 1σ uncertainties. The vertical blue dashed line shows the richness threshold at which the slope of the distribution changes (see § 2.4 and equation 4). Right: Red circles and uncertainties are as on left. Also shown are the mean masses of clusters from two simulations (see 2.4) Black points show clusters from mini-Uchuu with a subhalo peak velocity threshold of $v_{\text{peak}} = 130 \text{ km s}^{-1}$ and blue points show clusters from TNG with a galaxy stellar mass threshold of $M_s \geq 5 \times 10^9 h^{-1} M_{\odot}$. As can be seen clearly from both panels, a flattening (tail) of the MRR occurs at low richness ($\log N \lesssim 1.23$). The short tail in the simulations is not intrinsic. It is partially due to the threshold of simulations as well as Poisson scattering (see § A2).

in the cluster, N_{tot} , is equal to the number of members within R_{200} , N_{200} , plus the number of interlopers, N_{int} . In order to remove contamination by these interlopers we calculated the surface density profile of each cluster from its center and fit it with the King equation, defined as

$$\Sigma_{\text{tot}}(R) = \Sigma_c \left(1 + \frac{R^2}{r_c^2} \right)^{\nu} + \Sigma_{\text{int}}, \quad (3)$$

where Σ_c and Σ_{int} are the central and interlopers surface number densities and r_c is a scale radius. We apply equation 3 to all members assigned by the GalWeight technique within $6 h^{-1} \text{ Mpc}$, which is sufficiently large enough to take into account the effect of interlopers. Then, we integrate equation 3 to estimate the contribution of N_{int} .

The gray points in the left panel of Figure 2 show the distribution of the 1800 clusters in the GalWCat19 catalog in the mass-richness plane. Visual inspection shows that there is a large scatter in the relationship between mass and richness at the low-richness end. This is due to the large uncertainties introduced when calculating each cluster’s mass using a dynamical method when only a handful of member galaxy redshifts are available. The black points show the complete fiducial (\mathcal{S}_{fid}) subsample of 756 clusters to which the redshift selection function has been applied ($\log M_{200} \geq 13.9 h^{-1} M_{\odot}$ and $0.045 \leq z \leq 0.125$; see § 3.2). The mean mass of clusters in \mathcal{S}_{fid} as a function of their richness are shown as solid red circles, with error bars indicating 1σ Poisson uncertainties. The left panel of Figure 2 shows that when

mean mass is plotted as a function of richness, a distinct curve or “tail” appears to the otherwise linear relationship at the high-richness end. In other words, the MRR has a shallow slope at the low-richness end, while at the high-richness end the relation has a steep slope. Thus, there is a characteristic richness below which the trend changes. We call this characteristic richness threshold N_{th} .

In the following section, we study two numerical simulations and demonstrate that this tail is not intrinsic. We also demonstrate that it is possible to remove the effect of the tail when deriving the MRR by selecting a subsample of clusters with richness greater than a certain threshold (N_{th}). This threshold is dependent on the cluster catalog being utilized e.g., Baxter et al. (2016) and Murata et al. (2019) adopted $N_{\text{th}} = 20$ for the redMaP-Per cluster catalog (Rykoff et al. 2016) which utilizes red member galaxies, photometrically-selected from the SDSS-DR8 catalog. In § 2.5, we show how to apply a Hinge function to optimally determine N_{th} appropriate for any catalog. Using this method, we derive an optimal threshold of $N_{\text{th}} = 17$ (13) for all (red) member galaxies in the GalWCat19 catalog.

2.4. Simulations

As discussed in § 2.3, the MRR derived from the GalWCat19 cluster catalog shows a tail at the low-richness end. In this section we analyze two simulations to show that this tail is not intrinsic. The first simulation is the TNG300-1 simulation from the Illustris TNG300 suite (Pillepich et al. 2018; Nelson et al. 2019). The TNG300-

1 simulation contains 2500^3 dark matter (DM) particles and the same number of baryonic resolution elements in a box of comoving length $205 h^{-1}$ Mpc. It evolves from redshift $z = 127$ down to $z = 0$ using the AREPO moving-mesh code (Springel 2010; Weinberger et al. 2020), which solves the coupled equations of ideal magneto-hydrodynamics and self-gravity, taking magnetic fields into consideration. It assumes a standard Λ CDM cosmology, with $\Omega_\Lambda = 0.691$, $\Omega_m = 0.309$, $\Omega_b = 0.0486$, $h = 0.6777$, $n_s = 0.9667$, and $\sigma_8 = 0.8159$ (Planck Collaboration et al. 2016). The dark matter mass resolution is $4.0 \times 10^7 h^{-1} M_\odot$ and the baryonic mass resolution is $0.75 \times 10^7 h^{-1} M_\odot$. The gravitational softening lengths for dark matter and stars in TNG300-1 is $1.0 h^{-1}$ kpc. In this study, we use the snapshot #92 at redshift $z = 0.08$, which most closely matches the mean redshift ($z = 0.089$) of clusters in the GalWCat19 catalog.

The second simulation is the mini-Uchuu simulation from the Uchuu suite of large, high-resolution N -body simulations (Ishiyama et al. 2021) which were done for the Planck2016 cosmology (Planck Collaboration et al. 2016). Mini-Uchuu is a cosmological N -body simulation of 2560^3 particles in a box of co-moving length $400 h^{-1}$ Mpc, mass resolution of $3.27 \times 10^8 h^{-1} M_\odot$, and gravitational softening length of $4.27 h^{-1}$ kpc. Mini-Uchuu was created using the massively parallel N -body TreePM code, GREEM (Ishiyama et al. 2009, 2012). Haloes and subhaloes were identified with ROCKSTAR (Behroozi et al. 2013a) and merger trees constructed with CONSISTENT TREES (Behroozi et al. 2013b). Halo/subhalo catalogs and their merger trees are publicly available through the Skies & Universes site.⁴ Full details of the Uchuu simulation suite may be found in Ishiyama et al. (2021). Here, we analyze a snapshot at redshift $z \sim 0.09$. Note that in order to be consistent with how the GalWCat19 cluster masses are calculated, in the case of both simulations we define the cluster mass M_{200} as the mass enclosed within an overdensity of $200\rho_c$, where ρ_c is the critical density of the Universe.

The right panel of Figure 2 shows the MRR obtained from the Illustris-TNG (blue) and mini-Uchuu (black) simulations, as well as from the fiducial GalWCat19 cluster catalog, \mathcal{S}_{fid} (red). For the mini-Uchuu simulations we count all subhalos (galaxies) with a threshold of peak velocity $v_{\text{peak}} = 130 \text{ km s}^{-1}$ (equivalent to stellar mass of $\sim M_s = 5 \times 10^9 h^{-1} M_\odot$ and luminosity $\sim 0.4L_*$). For the Illustris-TNG halos (clusters) we determine the number of galaxies with a threshold of stellar mass $M_s = 5 \times 10^9 h^{-1} M_\odot$ within r_{200} . Note that for both simulations we select all clusters with masses $\log M_{200} \geq 13.9 h^{-1} M_\odot$. As can be seen from the right panel, there is very good agreements between the GalWCat19 MRR and those derived from both Uchuu and TNG at high richness ($N \gtrsim 17$, or $\log N \geq 1.23$). However, as can clearly also be seen from the right panel, a flattening (tail) of the MRR occurs for both simulations at low richness ($\log N \leq 1.23$). In appendix A2 we show that the length of the tail for both simulations depends on the adopted v_{peak} or M_s thresholds. This indicates that the tail is an artifact introduced by the selection applied (v_{peak} , or equivalently M_s), and is, therefore, not

real. It is partially due to the threshold of simulations as well as Poisson scattering

Thus, the tail in the MRR obtained from GalWCat19 is not intrinsic and the effect at low richness is due to the Poisson scattering, the systematics of determining the member galaxies and richness, calculating cluster masses of a small members galaxies, and the projection effect. We note that there are very good agreements with MRR obtained from GalWCat19 and both Uchuu and TNG at $N \gtrsim 17$. We conclude that it is necessary to apply a cut in richness. In § 2.5 we describe a process for determining the optimal value of richness at which to make the cut.

2.5. Selecting the richness threshold

We wish to determine the optimal richness threshold to apply in order to remove the effect of the tail described in § 2.4 and Figure 2. After identifying this value, the MRR can be derived for all clusters with richness larger than this threshold. In order to find the richness threshold N_{th} at which the slope of MRR changes we use the Hinge function defined as

$$Y = a + b_0(X - X_0) + (b - b_0)\delta \log \left(1 + \exp \frac{X - X_0}{\delta} \right), \quad (4)$$

where $Y = \log M_{200}$ and $X = \log N_{200}$. We use this function only to determine X_0 , which in our case is the richness threshold N_{th} .

Applying the Hinge function to the fiducial sample, \mathcal{S}_{fid} (§ 2.5), we find that the threshold at which the MRR changes its slope is $N_{\text{th}} = 17$ for all members and $N_{\text{th}} = 13$ for red members. The blue solid line in the left panel Figure 2 shows the Hinge function for \mathcal{S}_{fid} for all members, with the dotted blue lines indicating 1σ uncertainties. The vertical blue dashed line shows the optimal richness threshold of $N_{\text{th}} = 17$, derived for all members. In summary, we select all clusters with $\log M_{200} \geq 13.9 [h^{-1} M_\odot]$, $0.045 \leq z \leq 0.125$, in addition to $N_{\text{th}} = 17$ for all members and $N_{\text{th}} = 13$ for red members within R_{200} to derive MRR and cosmological constraints on Ω_m and σ_8 . We call these two subsamples $\mathcal{S}_{\text{all}17}$ and $\mathcal{S}_{\text{red}13}$. In § 4.3 we investigate the systematics of adopting N_{th} on our results.

3. THE MASS-RICHNESS RELATION

In this section we introduce our methodology for fitting the MRR, and then we apply it to the fiducial GalWCat19, $\mathcal{S}_{\text{all}17}$ and $\mathcal{S}_{\text{all}13}$ to derive the best-fit parameters of normalization α , slope β , and intrinsic scatter σ_{int} .

3.1. Methodology of fitting the mass-richness relation

The probability distribution of the mass of halos with a fixed richness N is given by a lognormal distribution (e.g., Saro et al. 2015; Simet et al. 2017; Chiu et al. 2020) as

$$P(\log M|N, z) = \frac{1}{\sqrt{2\pi\sigma_{\log M, N}^2}} \times \exp \left[-\frac{(\log M - \langle \log M|N \rangle)^2}{2\sigma_{\log M, N}^2} \right], \quad (5)$$

⁴ <http://www.skiesanduniverses.org/Simulations/Uchuu/>

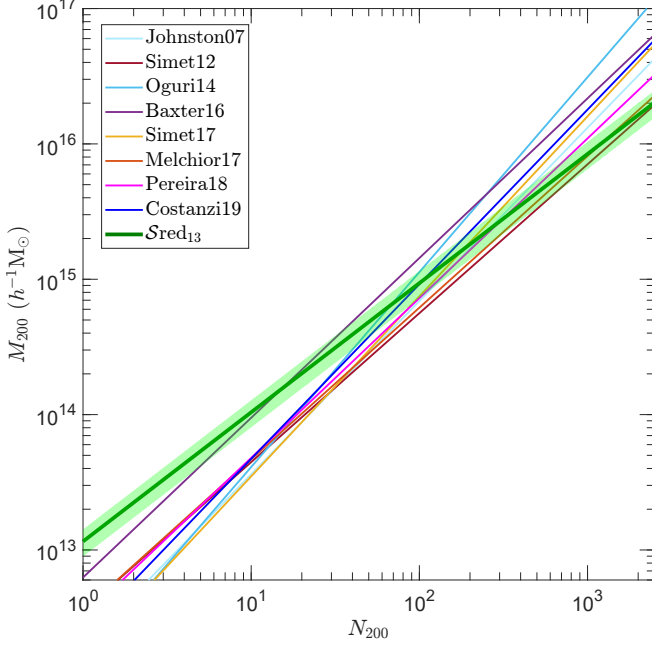


Figure 3. Comparison of the best-fit red MRR, MRR_{red} , derived in this work from $S_{\text{red}13}$ (dark green line with shading indicating 1σ uncertainty) with results reported in the literature (see legend and Table 2).

where the mean mass $\langle \log M|N \rangle$ is given as

$$\langle \log M|N \rangle = \alpha + \beta \log N, \quad (6)$$

In addition, the total variance in the mass $\sigma_{\log M, N}^2$ at a fixed richness, including contributions of the richness measurement errors \sqrt{N} , mass measurement errors $\sigma_{\log M}$, and the intrinsic scatter in mass σ_{int} , is modeled by

$$\sigma_{\log M, N}^2 = \frac{\beta^2}{N^2} + \sigma_{\log M}^2 + \sigma_{\text{int}}^2 \quad (7)$$

where α is the normalization and β is the slope of the mass-richness relation. Note that we ignore the evolution term in the MRR relation (Equation 6) because our redshift range is very small (0.045-0.0125) and including this term does not affect our results. We estimate the model parameters α , β , and σ_{int} with the affine-invariant Markov chain Monte Carlo (hereafter MCMC) sampler of Goodman & Weare (2010) as implemented in the MATLAB package GWCMC⁵ inspired by the python package `emcee` (Foreman-Mackey et al. 2013).

Using Markov Chain Monte Carlo (MCMC) fitting we now derive best-fit parameters for the MRR within R_{200} . For $S_{\text{all}17}$ we get $\alpha = 12.98 \pm 0.04 [h^{-1} M_{\odot}]$, $\beta = 0.96 \pm 0.03$, and $\sigma_{\text{int}} = 0.12 \pm 0.01$. For $S_{\text{red}13}$ we obtain $\alpha = 13.08 \pm 0.03 [h^{-1} M_{\odot}]$, $\beta = 0.95 \pm 0.02$, and $\sigma_{\text{int}} = 0.11 \pm 0.01$. In § 4.3, we discuss the systematics of adopting the redshift, mass, and richness thresholds on our best-fit estimates of the MRR relation.

3.2. Comparison to previous results

Table 2 compares our best-fit parameters for the red MRR (MRR_{red}) to those previously published by other groups who analysed different cluster catalogs (see also

Figure 3). We note that the normalization and slope of our MRR are noticeably different from other analyses. This is because we derived the MRR from the spectroscopic galaxy cluster catalog while other studies used photometric catalogs. As we discussed in the introduction, photometric catalogs have large systematical uncertainties because distances inferred from photometric redshift estimates are less accurate than those inferred from spectroscopic redshifts which increases the systematics of projection effect. Moreover, cluster catalogs constructed from photometric surveys do not return an estimate of each cluster’s mass directly. The masses of these clusters are calibrated via stacking clusters with the same richness and following up a subset of clusters with known masses which are calculated individually using different mass estimators such as weak lensing or X-ray observations (e.g., Simet et al. 2017).

Also, both the table and the figure demonstrate significant differences in the best-fit parameters amongst the different studies, even for those studies that analyzed the same catalogs e.g., Johnston et al. (2007) and Simet et al. (2012) who utilized the SDSS-MaxBCG catalog of Koester et al. 2007, and Baxter et al. (2016), Simet et al. (2017), and Costanzi et al. (2019) who utilized the SDSS-redMaPPER catalog.

The tension in the MRR parameters obtained from different studies can be explained as follows. In deriving the MRR it is necessary to independently calculate the richness and the mass of each cluster. On one hand, estimating cluster richness is complicated. It depends on the cluster-finder method, the projection effect, the completeness of the sample, the definition of the cluster richness, cluster evolution, and the aperture within which the richness is calculated. On the other hand, calculating cluster mass is also complicated. Cluster masses can be calculated by the virial mass estimator, weak gravitational lensing and X-ray observations. However, these methods often return biased results owing to the assumption of hydrostatic equilibrium, projection effect, possible velocity anisotropies in galaxy orbits, the assumption that halo mass follows light (or stellar mass), the presence of substructure and/or nearby structure, the presence of interlopers in the cluster frame (see, e.g., Tonry & Davis 1981; The & White 1986; Fadda et al. 1996; Abdullah et al. 2013; Zhang et al. 2019).

In addition to aforementioned factors, the size of the subsample used for the MRR calibration is usually small (tens of clusters), which introduces large uncertainties in both the slope and the normalization of the MRR relation. Moreover, many cluster catalogs span a large redshift range, so evolution (due to both the evolution of the universe and the physical processes of baryons in clusters) in the scaling relations used to estimate the masses needs to be carefully handled, introducing another source of uncertainty. Other observational systematics that introduce additional uncertainties are photometric redshift errors and cluster miscentering. All of the aforementioned factors can introduce significant uncertainties in the estimates of both the cluster richness and mass and consequently the constraints on MRR parameters (e.g., Henry et al. 2009; Mantz et al. 2015) and Ω_m and σ_8 parameters as well (see § 4.1 and Figure 4).

⁵ <https://github.com/grinsted/gwcmc>

Table 2

Comparison of best-fit parameters for the red mass-richness relation (MRR_{red}) derived here with previously published values using different catalogs. All parameters have been calibrated to pivotal richness $N_{\text{piv}} = 1$.

Reference	sample-membership	10^α ($10^{12} h^{-1} M_\odot$)	β	redshift
Johnston et al. (2007)	photo-SDSS-MaxBCG ^(a)	1.90 ± 0.26	1.28 ± 0.04	0.10 – 0.30
Simet et al. (2012)	photo-SDSS-MaxBCG	3.54 ± 0.28	1.10 ± 0.12	0.10 – 0.30
Oguri (2014)	photo-SDSS-CAMIRA ^(b)	1.25 ± 0.15	1.44 ± 0.27	0.10 – 0.60
Baxter et al. (2016)	photo-SDSS-redMaPPer ^(c)	4.84 ± 0.96	1.18 ± 0.16	0.18 – 0.33
Simet et al. (2017)	photo-SDSS-redMaPPer	1.64 ± 0.12	1.33 ± 0.09	0.10 – 0.33
Melchior et al. (2017)	photo-DES-redMaPPer ^(d)	3.55 ± 0.57	1.12 ± 0.20	0.20 – 0.80
Pereira et al. (2018)	photo-SDSS-redMaPPer	3.17 ± 0.12	1.18 ± 0.09	0.10 – 0.33
Costanzi et al. (2019)	photo-SDSS-redMaPPer	2.42 ± 0.17	1.29 ± 0.09	0.10 – 0.30
This work ($S_{\text{red}13}$)	Spec-SDSS-GalWCat19	11.4 ± 0.16	0.95 ± 0.02	0.045 – 0.125

(a) A red-sequence cluster finder (Koester et al. 2007). (b) CAMIRA = Cluster finding algorithm based on Multi-band Identification of red galaxies. (c) Baxter et al. (2016) used a subsample of SDSS redMaPPer cluster catalog (Rykoff et al. 2014) which is in the North Galactic Cap (NGC). Here $\log(M_0)$ is calculated at $z = 0.089$ (mean redshift of GalWCat19). (d) Melchior et al. (2017) used DES (Dark Energy Survey) redMaPPer cluster catalog (Rykoff et al. 2016). Here $\log(M_0)$ is calculated at $z = 0.089$. (e) Pereira et al. (2018) used 230 redMaPPer clusters obtained from Rykoff et al. (2016) and 136 VT clusters obtained from Wiesner et al. (2015)

4. IMPLICATIONS FOR COSMOLOGICAL MODELS AND CONSTRAINING Ω_m AND σ_8

In this section we summarize our procedure for constraining Ω_m and σ_8 . We start with calculating the halo (cluster) mass function (HMF) from theory, comparing with the CMF we obtain from the MRR relation, and then constraining Ω_m and σ_8 . Full details may be found in Abdullah et al. (2020a).

4.1. Prediction of Halo Mass Function (HMF)

The number of clusters per unit mass per unit comoving volume of the universe is given by

$$\frac{dn}{d \ln M} = f(\sigma) \frac{\rho_0}{M} \left| \frac{d \ln \sigma}{d \ln M} \right|, \quad (8)$$

where ρ_0 is the mean density of the universe, σ is the rms mass variance on a scale of radius R that contains a mass $M = 4\pi\rho_0 R^3/3$, and $f(\sigma)$ represents the functional form that defines a particular HMF fit. We adopt the functional form of Tinker et al. (2008) (hereafter Tinker08) to calculate the HMF and consequently the predicted abundance of clusters. The Tinker08 function is given by

$$f(\sigma, z) = A \left[\left(\frac{\sigma}{b} \right)^{-a} + 1 \right] \exp(-c/\sigma^2) \quad (9)$$

where $A = 0.186(1+z)^{-0.14}$, $a = 1.47(1+z)^{-0.06}$, $b = 2.57(1+z)^{-\alpha}$, $c = 1.19$, and $\ln \alpha(\Delta_{\text{vir}}) = [75/(\ln(\Delta_{\text{vir}}/75))]^{1.2}$, and σ^2 is the mass variance defined as

$$\sigma^2(M, z) = \frac{g(z)}{2\pi} \int P(k) W^2(kR) k^2 dk \quad (10)$$

$P(k)$ is the current linear matter power spectrum (at $z = 0$) as a function of wavenumber k , $W(kR) = 3[\sin(kR) - kR \cos(kR)]/(kR)^3$ is the Fourier transform of the real-space top-hat window function of radius R , and $g(z) = \sigma_8(z)/\sigma_8(0)$ is the growth factor of linear perturbations at scales of $8h^{-1}$ Mpc, normalized to unity at $z = 0$. For more details regarding calculation of the HMF we refer the reader to e.g., Press & Schechter (1974); Tinker & Wetzel (2010); Behroozi et al. (2013a); Shirasaki et al. (2021).

We calculate the predicted HMF by allowing Ω_m to vary between [0.1, 0.6] and σ_8 between [0.6, 1.2], in both cases in steps of 0.005. We keep the following cosmological parameters fixed: the CMB temperature $T_{\text{cmb}} = 2.725 K^\circ$, baryonic density $\Omega_b = 0.0486$, and spectral index $n = 0.967$ (Planck Collaboration et al. 2014), at redshift $z = 0.089$ (the mean redshift of GalWCat19).

In order to calculate the CMF from observation we begin by deriving MRR relations for both $S_{\text{all}17}$ and $S_{\text{red}13}$ subsamples. We then estimate the mass of each cluster knowing its richness and calculate the CMF from observations. The CMF is calculated for clusters with masses $\log M_{200} \geq 13.9 [h^{-1} M_\odot]$ and in the redshift range of $0.045 \leq z \leq 0.125$. Abdullah et al. (2020b) showed that, for clusters in the redshift range of $0.045 \leq z \leq 0.125$, the effect of evolution on the HMF is less than 3%. Note that in this work, rather than utilizing the dynamically-derived estimate of cluster mass in GalWCat19, we re-estimate each cluster mass from its richness using the best-fit MRR and calculate the CMF from those masses.

Finally, in order to determine the best-fit mass function and constrain Ω_m and σ_8 we use a standard χ^2 procedure

$$\chi^2 = \sum_{i=1}^N \left(\frac{[y_{o,i} - y_{m,i}]^2}{\sigma_i^2} \right), \quad (11)$$

where the likelihood, $\mathcal{L}(y|\sigma_8, \Omega_m)$, of a data y_o given a model y_m is

$$\mathcal{L}(y|\sigma_8, \Omega_m) \propto \exp\left(\frac{-\chi^2(y|\sigma_8, \Omega_m)}{2}\right) \quad (12)$$

Note that σ includes the statistical uncertainty of the data plus the intrinsic scatter σ_{int} obtained from the MRR relation (equation 7).

4.2. Constraints on Cosmological Parameters Ω_m and σ_8

In this section we present the constraints we obtain on Ω_m and σ_8 using firstly the MRR derived for all members ($S_{\text{all}17}$) and then for red members ($S_{\text{red}13}$). We also compare the constraints we derive firstly to the cosmological constraints obtained from other groups who fit to MRR relations, and then to the cosmological constraints

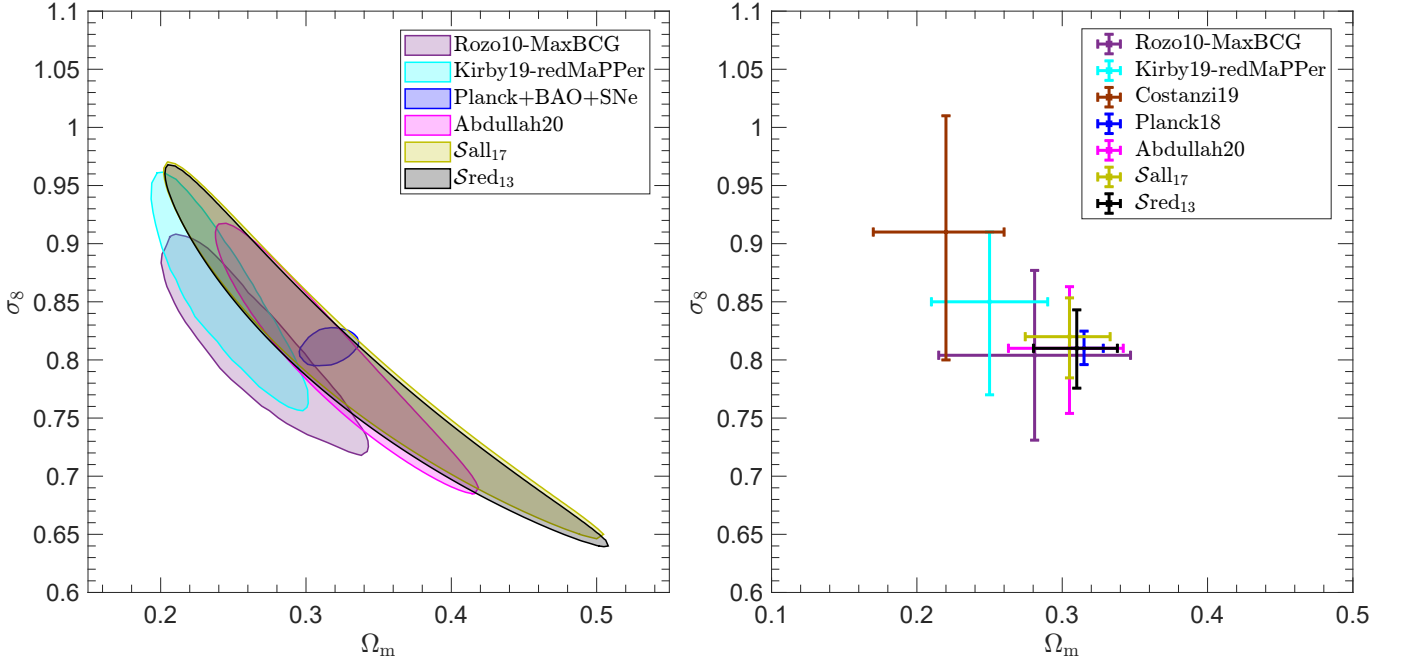


Figure 4. Comparison of constraints obtained on Ω_m and σ_8 in this work with those obtained from previous MRR analyses using different cluster catalogs and richness thresholds. Left: 68% CLs derived within R_{200} for all members with $N_{\text{th}} = 17$ (yellow, Sall₁₇) and red members with $N_{\text{th}} = 13$ (gray, Sred₁₃). Right: uncertainties on Ω_m and σ_8 estimated from the previous studies of Rozo et al. (2010); Costanzi et al. (2019); Kirby et al. (2019); Lesci et al. (2022) (purple, brown, cyan, respectively) which use the cluster abundance technique and cluster mass estimates from the mass-richness relation (CA_{MRR}). Also shown are Abdullah et al. (2020b) (pink) which uses the cluster abundance technique and cluster mass estimates from the dynamics of member galaxies (CA_{dyn}) and Planck Collaboration et al. (2018) (blue) which uses the CMB technique (see Table 1 for the abbreviation).

obtained from the Planck Collaboration et al. (2018) who utilized the CMB technique.

We derive the cosmological parameters Ω_m and σ_8 , as discussed in § 4.1, after estimating each cluster mass in either the full or red subsample using its MRR. Utilizing the subsample of clusters with all members, Sall₁₇, we obtain $\Omega_m = 0.31^{+0.03}_{-0.03}$ and $\sigma_8 = 0.82^{+0.03}_{-0.04}$. Utilizing the subsample of clusters with red members, Sred₁₃, we find $\Omega_m = 0.31^{+0.03}_{-0.03}$ and $\sigma_8 = 0.81^{+0.03}_{-0.03}$. Figure 4 shows our constraints on Ω_m and σ_8 using the subsamples Sall₁₇ and Sred₁₃, as well as previously published constraints from Rozo et al. (2010); Costanzi et al. (2019); Kirby et al. (2019); Abdullah et al. (2020b) which use the MRR (CA_{MRR}) or dynamical (CA_{dyn}) cluster abundance techniques and Planck Collaboration et al. (2018) which use the CMB technique (see Table 1 for more details). As shown in the figure, the 68% confidence levels (CLs) obtained from our catalogs Sall₁₇ (yellow) and Sred₁₃ (gray) are very consistent and overlap with each other. Our 68% CLs are also consistent with the 68% CLs obtained by the other groups. However, despite this overlapping, the right panel of Figure 4 shows that the constraints on Ω_m and σ_8 obtained from the CA_{MRR} techniques are in tension with each other. This tension comes from the discrepancy between the MRRs derived by the different studies as discussed in § 3.2. We end by noting that the constraints we derive on Ω_m and σ_8 here from the MRR agree very well both with the constraints derived by the Planck Collaboration et al. (2018) and Abdullah et al. (2020b) using the two independent techniques of CMB and cluster dynamics, respectively (although this work and Abdullah et al. (2020b) did utilize the same SDSS catalog). In § 4.3, we discuss the system-

atics on the the cosmological constraints introduced by adopting redshift, mass, and richness thresholds.

4.3. Systematics

In this section we discuss the systematics introduced when deriving the MRR and cosmological parameters due to the adoption of the cluster mass threshold $\log M_{200} \geq 13.9 [h^{-1} M_\odot]$, the lower and upper redshift thresholds $0.045 \leq z \leq 0.125$, and the richness thresholds $N_{\text{th}} = 17$ for Sall₁₇ and $N_{\text{th}} = 13$ for Sred₁₃.

The first systematic uncertainty comes from the difficulty of accurately determining the mass threshold at which the sample is mass complete. As discussed in Section § 3.2 the catalog is approximately complete around $\log M_{200} \gtrsim 13.9 [h^{-1} M_\odot]$. We investigate the effect of varying the mass threshold $\log M_{200}$ between 13.8 and 14.0 $[h^{-1} M_\odot]$ on the derived MRR and cosmological parameters from our analysis. For each mass threshold we calculate the χ^2 likelihood and then we obtain the joint 68% CL of all χ distributions as shown in Figure 5. The systematic uncertainties in MRR and cosmological parameters are listed in Table 3. Both the plot and the table show that the best-fit value of each parameter deviates very slightly from the results of the fiducial samples Sall₁₇ and Sred₁₃.

The second systematic uncertainty comes from the choice of the redshift interval. We first fix the upper redshift threshold to $z = 0.125$ and vary the lower redshift threshold from 0.01 to 0.07. Both Figure 5 and Table 3 indicate that varying the lower redshift threshold does not affect our result for the fiducial samples Sall₁₇ and Sred₁₃. It demonstrates that the evolution effect is unremarkable in this small redshift interval (see also Abdullah

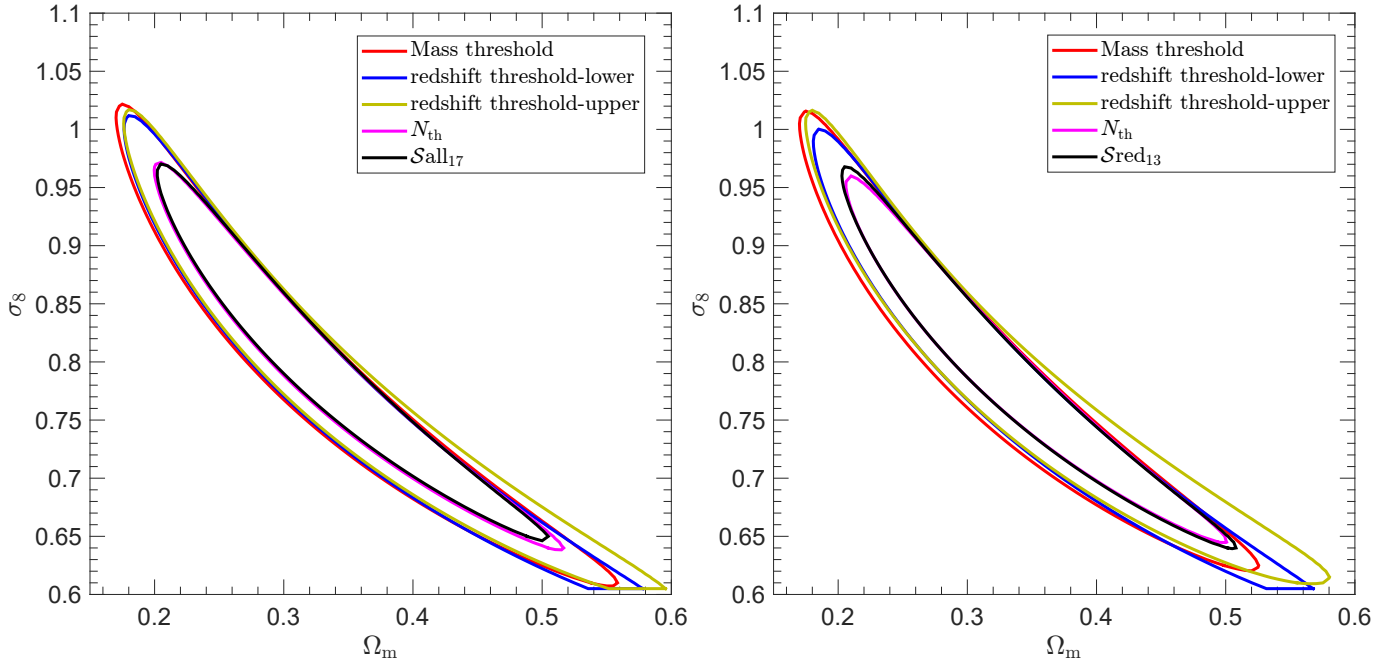


Figure 5. Systematical effects of cluster mass, lower and upper redshifts, and richness thresholds on our constraints on the cosmological parameters for the analysis on the fiducial samples of $\mathcal{S}_{\text{all}17}$ for all members within R_{200} (left) and $\mathcal{S}_{\text{red}13}$ for red members within R_{200} (right) (see § 4.3 for details). The 68% CLs for our fiducial sample, varying mass threshold $\log M_{200}$ between 13.8 and 14.0 [$h^{-1} M_{\odot}$], fixing the upper redshift threshold to 0.125 and varying the lower redshift threshold from 0.01 to 0.07, fixing the lower redshift threshold to 0.045 and varying the upper redshift threshold from 0.11 to 0.15, varying N_{th} from 15 to 19 for $\mathcal{S}_{\text{all}17}$, and varying N_{th} from 13 to 17 for $\mathcal{S}_{\text{red}13}$.

Table 3

Dependence of MRR and cosmological parameters on mass, lower and upper redshifts, and richness thresholds (§ 4.3).

	sample	threshold range	α	β	Ω_m	σ_8
Mass threshold	all	$\log M_{200,\text{th}} = [13.8 - 14.0]$	12.97 ± 0.10	0.96 ± 0.06	0.30 ± 0.03	0.82 ± 0.02
Mass threshold	red	$\log M_{200,\text{th}} = [13.8 - 14.0]$	13.06 ± 0.10	0.96 ± 0.06	0.30 ± 0.02	0.81 ± 0.03
redshift lower threshold	all	$z_{\text{th}} = [0.01 - 0.07]$	12.97 ± 0.01	0.96 ± 0.01	0.31 ± 0.01	0.81 ± 0.02
redshift lower threshold	red	$z_{\text{th}} = [0.01 - 0.07]$	13.07 ± 0.01	0.95 ± 0.01	0.31 ± 0.01	0.81 ± 0.01
redshift upper threshold	all	$z_{\text{th}} = [0.10 - 0.15]$	13.01 ± 0.11	0.93 ± 0.05	0.33 ± 0.05	0.80 ± 0.07
redshift upper threshold	red	$z_{\text{th}} = [0.10 - 0.15]$	13.13 ± 0.13	0.91 ± 0.07	0.34 ± 0.09	0.80 ± 0.08
richness threshold	all	$N_{\text{th}} = [15 - 19]$	12.98 ± 0.10	0.96 ± 0.06	0.31 ± 0.03	0.82 ± 0.04
richness threshold	red	$N_{\text{th}} = [11 - 15]$	13.10 ± 0.10	0.94 ± 0.05	0.32 ± 0.03	0.81 ± 0.03

et al. 2020b). We then fix the lower redshift threshold to $z = 0.045$ and vary the upper redshift threshold from 0.10 to 0.15. The best-fit value of each parameter deviates slightly from the results of the fiducial samples $\mathcal{S}_{\text{all}17}$ and $\mathcal{S}_{\text{red}13}$.

The third systematic uncertainty comes from the choice of the richness threshold N_{th} . Therefore, we investigate the effect of varying N_{th} between 15 and 19 for $\mathcal{S}_{\text{all}17}$ and N_{th} between 13 and 17 for $\mathcal{S}_{\text{red}13}$ on the derived MRR and cosmological parameters. Both Figure 5 and Table 3 show that the best-fit value of each parameter deviates very slightly from the results of the fiducial samples $\mathcal{S}_{\text{all}17}$ and $\mathcal{S}_{\text{red}13}$.

5. CONCLUSION

In this paper, we derive the mass-richness relation (MRR) and constrained the cosmological parameters Ω_m and σ_8 from the GalWCat19 cluster catalog (Abdullah et al. 2020b), which was constructed from the SDSS-DR13 spectroscopic data set. The advantages of using GalWCat19 are (i) we were able to identify clusters, assign

membership, and determine cluster centers and redshifts with high accuracy from the high-quality SDSS spectroscopic data set; (ii) cluster membership was determined by the GalWeight technique, which has been shown to be $\sim 98\%$ accurate in assigning cluster membership (Abdullah et al. 2018); (iii) cluster masses were calculated individually using the virial theorem and corrected for the surface pressure term; (iv) GalWCat19 is a low-redshift cluster catalog which eliminates the need to make any assumptions about evolution in cluster mass or evolution in cosmological parameters. We select two cluster subsamples $\mathcal{S}_{\text{all}17}$ with richness threshold $N_{\text{th}} = 17$ for all members and $\mathcal{S}_{\text{red}13}$ with $N_{\text{th}} = 13$ for red members both within R_{200} and with $\log M_{200} \geq 13.9 [h^{-1} M_{\odot}]$, $0.045 \leq z \leq 0.125$. We summarize our findings below:

1. The MRR shows a tail at low-richness. Using the Illustris-TNG and mini-Uchuu cosmological numerical simulations, we find that this tail is caused by systematical uncertainties. Benchmarking both against Illustris-TNG and mini-Uchuu numerical

simulations, we find that, with a judicious choice of richness threshold, cluster richness scales tightly with cluster mass (see Figure 2). We conclude that the MRR is a powerful and effective tool for estimating cluster mass and for deriving cosmological constraints from cluster catalogs.

2. Using MCMC fitting (§ 3.1) we derive the best-fit parameters of the MRR within R_{200} (§ 3). For \mathcal{S}_{all17} we find $\alpha = 12.98 \pm 0.04 [h^{-1} M_{\odot}]$, $\beta = 0.96 \pm 0.03$, and $\sigma_{int} = 0.12 \pm 0.01$. For \mathcal{S}_{red13} we obtain $\alpha = 13.08 \pm 0.03 [h^{-1} M_{\odot}]$, $\beta = 0.95 \pm 0.02$, and $\sigma_{int} = 0.11 \pm 0.01$.
3. The slope of our MRR is consistent with both the Illustris-TNG and mini-Uchuu numerical simulations while MRRs derived from photometric catalogs return a steeper slope. This is likely because we derived our MRR from a spectroscopic galaxy cluster catalog while the other works used photometric catalogs. Photometric redshifts are known to be less accurate than those determined from spectroscopic redshifts. This increases the incidence of line-of-sight galaxies in close projection which are falsely-assigned as cluster members.
4. We estimate a mass for each cluster in the GalWCat19 catalog using the MRR relation and then derive constraints on the cosmological parameters Ω_m and σ_8 using the cluster abundance technique (§ 4.1 and § 3.1). Using the MRR determined from all members, we obtain $\Omega_m = 0.31^{+0.03}_{-0.03}$ and $\sigma_8 = 0.82^{+0.03}_{-0.04}$, and for red members, \mathcal{S}_{red13} we obtain $\Omega_m = 0.31^{+0.03}_{-0.03}$ and $\sigma_8 = 0.81^{+0.03}_{-0.03}$. We compare our results to Rozo et al. (2010); Costanzi et al. (2019); Kirby et al. (2019); Lesci et al. (2022) who also used the cluster abundance technique and mass-richness relation (CA_{MRR}). We also compare our results to Abdullah et al. (2020b) who used the cluster abundance technique and galaxy dynamics technique (CA_{dyn}) and with Planck Collaboration et al. (2018) who used the CMB technique (see Table 1 for the abbreviation). We find that the constraints we derive from \mathcal{S}_{all17} and \mathcal{S}_{red13} are consistent and overlap with each other. Reassuringly, the constraints we obtain on Ω_m and σ_8 are consistent with those obtained both by Planck Collaboration et al. (2018) and Abdullah et al. (2020b) using independent techniques.
5. We discuss the systematics of adopting mass, redshift, and richness thresholds when deriving our MRR and cosmological parameters (§ 4.3). We find that the best-fit value of each parameter deviates only slightly from those of the two fiducial samples of \mathcal{S}_{all17} and \mathcal{S}_{red13} (Figure 4 and Table 3).

In future work we aim to (i) investigate the stellar mass and luminosity function of member galaxies; (ii) study the connection between stellar mass (or luminosity) and cluster mass; (iii) investigate the environmental effects on the properties of member galaxies such as size, color, and star formation rate; and (iv) study the correlation function of galaxy clusters and

the signature of baryonic acoustic oscillations to constrain cosmological parameters utilizing both the low-redshift spectroscopic GalWCat19 cluster catalog and the recent public data releases of the Uchuu-SDSS galaxy lightcones (Dong-Páez et al. 2022), the Uchuu- ν^2 GC semi-analytic galaxy/AGN (Oogi et al. 2022), and the Uchuu-UniverseMachine galaxy catalogues (Aung et al. 2022). We also look forward to apply the Fog-GalWeight (see Abdullah et al. 2018, 2020a) toolkit to the ongoing and upcoming high-redshift spectroscopic surveys such as DESI (Levi et al. 2019), Euclid (Euclid Collaboration et al. 2019), SPHEREX (Doré et al. 2014), and Subaru Prime Focus Spectrograph (PFS) (Takada et al. 2014).

We gratefully acknowledge support from the Japan Society for the Promotion of Science through JSPS KAKENHI Grant Number JP21F51024. We gratefully acknowledge support from the National Science Foundation through grant AST-2205189, and from HST program numbers GO-15294 and GO-16300. Support for program numbers GO-15294 and GO-16300 was provided by NASA through grants from the Space Telescope Science Institute, which is operated by the Association of Universities for Research in Astronomy, Incorporated, under NASA contract NAS5-26555. T.I. has been supported by IAAR Research Support Program in Chiba University Japan, MEXT/JSPS KAKENHI (Grant Number JP19KK0344 and JP21H01122), MEXT as “Program for Promoting Researches on the Supercomputer Fugaku” (JPMXP1020200109), and JICFuS. We thank Instituto de Astrofísica de Andalucía (IAA-CSIC), Centro de Supercomputación de Galicia (CESGA) and the Spanish academic and research network (RedIRIS) in Spain for hosting Uchuu Data Release one in the Skies & Universes site for cosmological simulations. The Uchuu simulations were carried out on Aterui II supercomputer at Center for Computational Astrophysics, CfCA, of National Astronomical Observatory of Japan, and the K computer at the RIKEN Advanced Institute for Computational Science. The Uchuu DR1 effort has made use of the skun@IAA.RedIRIS and skun6@IAA computer facilities managed by the IAA-CSIC in Spain (MICINN EU-Feder grant EQC2018-004366-P).

A1. SEPARATING RED AND BLUE GALAXIES

In this section we describe our procedure to identify the red-sequence galaxies of GalWCat19 members. It is well known that clusters are dominated by elliptical, red E/S0 galaxies which occupy a narrow region in color-magnitude diagram (CMD) known as the E/S0 ridgeline or red-sequence (e.g., Bower et al. 1992; Gladders & Yee 2000). The location and the slope of this ridgeline in color decreases smoothly with increasing redshift (Koester et al. 2007). The GalWCat19 catalog contains clusters in the redshift range $0.01 \leq z \leq 0.2$. In order to identify red members, we sort the clusters into 14 equally-sized redshift bins, each approximately spanning $\Delta z = 0.01$. Then, for each redshift bin, we plot the members in the rest-frame $g - r$ vs M_r CMD to identify the ridgeline. The ridgeline is defined to be the line with maximum likelihood (or pdf) in color for the distribution of galaxies in the CMD (see the first two nested panels in Figure A1). This ridgeline can be located using the

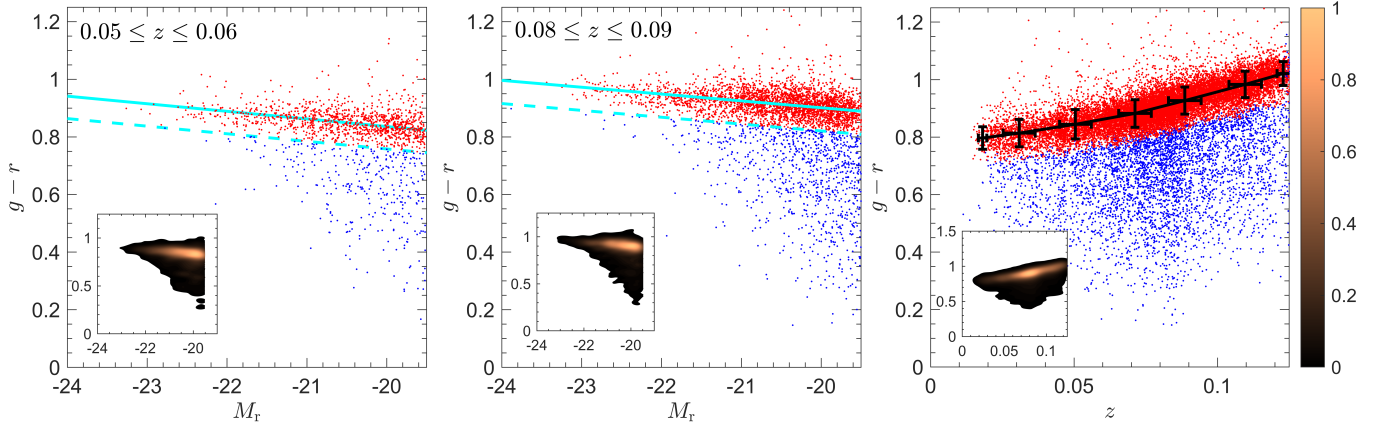


Figure A1. Separating red and blue members of the GalWCat19 clusters using the color-magnitude diagram (CMD). The left and middle panels show the CMD for cluster members in two different redshift bins. The solid cyan line in each panel shows the red-sequence ridgeline (highest probability) and the dashed line is the line that separates red and blue members at the 1σ CL from the ridgeline. The right panel shows the evolution of the ridgeline as a function redshift. The black line shows the mean color of the red members as a function of redshift with 1σ uncertainties. The nested panels show the probability distribution functions for galaxies in the CMD.

two-dimensional adaptive kernel method (2DAKM, see e.g. Pisani 1996) or the Gaussian Mixture Model for red-sequence galaxy identification (Hao et al. 2009). In this paper we apply the 2DAKM to identify the location of the ridgeline. We then locate the line with probability of 1σ CL below the ridgeline. We define red galaxies as those with rest-frame color above the 1σ line.

Figure A1 shows the CMD of GalWCat19 galaxies at two redshift bins $0.05 \leq z \leq 0.06$ and $0.08 \leq z \leq 0.09$. The solid cyan line in each panel represents the red-sequence ridgeline and the dashed line is the line that separates the red and blue galaxies with probability of 1σ CL from the ridgeline. In the right panel of Figure A1 we plot the color-redshift relation. The plot demonstrates that the slope of the ridgeline varies with redshift.

A2. IS THE MRR TAIL INTRINSIC?

In Figure A2, we plot the MRR relation for the mini-Uchuu and Illustris-TNG simulations. For the mini-Uchuu simulations we plot MRR for five v_{peak} thresholds for subhalos and for the Illustris-TNG halos we present MRR for four M_s thresholds for galaxies both within r_{200} . The figure shows a short tail at low-richness end. The tail increases with increasing the thresholds of v_{peak} for the Mini-Uchuu and M_s for TNG of the selected sample from each simulation. We conclude that this tail is not intrinsic and the effect at low richness is partially due to the threshold of simulations as well as Poisson scattering.

REFERENCES

- Abbott, T. M. C., Abdalla, F. B., Allam, S., et al. 2018, *ApJS*, **239**, 18
- Abdullah, M. H., Ali, G. B., Ismail, H. A., & Rassem, M. A. 2011, *MNRAS*, **416**, 2027
- Abdullah, M. H., Klypin, A., & Wilson, G. 2020a, *ApJ*, **901**, 90
- Abdullah, M. H., Praton, E. A., & Ali, G. B. 2013, *MNRAS*, **434**, 1989
- Abdullah, M. H., Wilson, G., & Klypin, A. 2018, *ApJ*, **861**, 22
- Abdullah, M. H., Wilson, G., Klypin, A., et al. 2020b, *ApJS*, **246**, 2
- Akeson, R., Armus, L., Bachelet, E., et al. 2019, arXiv e-prints, arXiv:1902.05569
- Albaret, F. D., Allende Prieto, C., Almeida, A., et al. 2017, *ApJS*, **233**, 25
- Aung, H., Nagai, D., Klypin, A., et al. 2022, arXiv e-prints, arXiv:2209.12918
- Battye, R. A., & Weller, J. 2003, *Phys. Rev. D*, **68**, 083506
- Baxter, E. J., Rozo, E., Jain, B., Rykoff, E., & Wechsler, R. H. 2016, *MNRAS*, **463**, 205
- Behroozi, P. S., Wechsler, R. H., & Wu, H.-Y. 2013a, *ApJ*, **762**, 109
- Behroozi, P. S., Wechsler, R. H., Wu, H.-Y., et al. 2013b, *ApJ*, **763**, 18
- Binney, J., & Tremaine, S. 1987
- Biviano, A., Murante, G., Borgani, S., et al. 2006, *A&A*, **456**, 23
- Blanton, M. R., & Roweis, S. 2007, *AJ*, **133**, 734
- Blanton, M. R., Hogg, D. W., Bahcall, N. A., et al. 2003, *ApJ*, **592**, 819
- Bocquet, S., Saro, A., Mohr, J. J., et al. 2015, *ApJ*, **799**, 214
- Bower, R. G., Lucey, J. R., & Ellis, R. S. 1992, *MNRAS*, **254**, 589
- Carlberg, R. G., Yee, H. K. C., & Ellingson, E. 1997, *ApJ*, **478**, 462
- Chiu, I. N., Umetsu, K., Murata, R., Medezinski, E., & Oguri, M. 2020, *MNRAS*, **495**, 428
- Costanzi, M., Rozo, E., Simet, M., et al. 2019, *MNRAS*, **488**, 4779
- Dahle, H. 2006, *ApJ*, **653**, 954
- Deason, A. J., Belokurov, V., & Sanders, J. L. 2019, *MNRAS*, **490**, 3426
- DES Collaboration, Abbott, T., Aguena, M., et al. 2020, arXiv e-prints, arXiv:2002.11124
- Dong-Páez, C. A., Smith, A., Szewciw, A. O., et al. 2022, arXiv e-prints, arXiv:2208.00540
- Doré, O., Bock, J., Ashby, M., et al. 2014, arXiv e-prints, arXiv:1412.4872
- Euclid Collaboration, Adam, R., Vannier, M., et al. 2019, *A&A*, **627**, A23
- Fadda, D., Girardi, M., Giuricin, G., Mardirossian, F., & Mezzetti, M. 1996, *ApJ*, **473**, 670
- Foreman-Mackey, D., Hogg, D. W., Lang, D., & Goodman, J. 2013, *PASP*, **125**, 306
- Giuricin, G., Mardirossian, F., & Mezzetti, M. 1982, *ApJ*, **255**, 361
- Gladders, M. D., & Yee, H. K. C. 2000, *AJ*, **120**, 2148
- Goodman, J., & Weare, J. 2010, *Communications in Applied Mathematics and Computational Science*, **5**, 65
- Hao, J., Koester, B. P., McKay, T. A., et al. 2009, *ApJ*, **702**, 745
- Henry, J. P., Evrard, A. E., Hoekstra, H., Babul, A., & Mahdavi, A. 2009, *ApJ*, **691**, 1307
- Holmberg, K., Schirmer, M., & Dahle, H. 2009, *A&A*, **504**, 1
- Ishiyama, T., Fukushige, T., & Makino, J. 2009, *PASJ*, **61**, 1319
- Ishiyama, T., Nitadori, K., & Makino, J. 2012, arXiv e-prints, arXiv:1211.4406
- Ishiyama, T., Prada, F., Klypin, A. A., et al. 2021, *MNRAS*, **506**, 4210
- Jackson, J. C. 1972, *MNRAS*, **156**, 1P

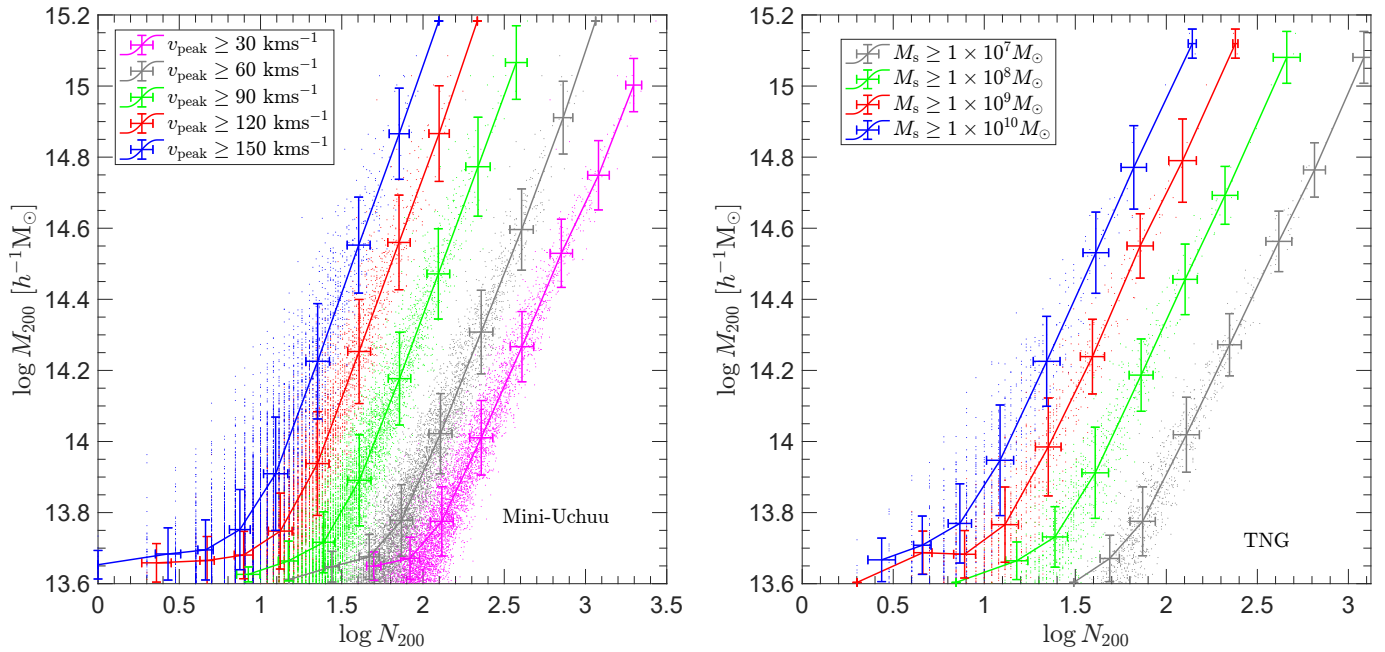


Figure A2. Mass-richness relation (MRR) for simulations. The mean mass at some richness bins is plotted for Mini-Uchuu (left) for five v_{peak} thresholds for subhalos and TNG (right) for four M_s thresholds for galaxies within r_{200} as shown in each legend. Error bars represent Poisson noise. The figure shows that MRR introduces a tail at low-richness end. The length of the tail increase with increases the thresholds of v_{peak} and M_s . This indicates that the tail is dependent on the selection of the threshold and it is not intrinsic.

- Johnston, D. E., Sheldon, E. S., Wechsler, R. H., et al. 2007, arXiv e-prints, arXiv:0709.1159
- Kaiser, N. 1987, *MNRAS*, **227**, 1
- Kauffmann, G., Colberg, J. M., Diaferio, A., & White, S. D. M. 1999, *MNRAS*, **303**, 188
- Kauffmann, G., Heckman, T. M., White, S. D. M., et al. 2003, *MNRAS*, **341**, 33
- Kirby, M., Rozo, E., Morris, R. G., et al. 2019, arXiv e-prints, arXiv:1910.13548
- Klypin, A., Yepes, G., Gottlöber, S., Prada, F., & Heß, S. 2016, *MNRAS*, **457**, 4340
- Koester, B. P., McKay, T. A., Annis, J., et al. 2007, *ApJ*, **660**, 239
- Lesci, G. F., Marulli, F., Moscardini, L., et al. 2022, *A&A*, **659**, A88
- Levi, M., Allen, L. E., Raichoor, A., et al. 2019, in BAAS, Vol. 51, 57
- Limber, D. N., & Mathews, W. G. 1960, *ApJ*, **132**, 286
- LSST Science Collaboration, Abell, P. A., Allison, J., et al. 2009, arXiv e-prints, arXiv:0912.0201 [astro-ph.IM]
- Mantz, A. B., von der Linden, A., Allen, S. W., et al. 2015, *MNRAS*, **446**, 2205
- Mantz, A. B., Allen, S. W., Morris, R. G., et al. 2016, *MNRAS*, **463**, 3582
- Melchior, P., Gruen, D., McClintock, T., et al. 2017, *MNRAS*, **469**, 4899
- Merloni, A., Predehl, P., Becker, W., et al. 2012, arXiv e-prints, arXiv:1209.3114
- Merritt, D. 1988, in Astronomical Society of the Pacific Conference Series, Vol. 5, The Minnesota lectures on Clusters of Galaxies and Large-Scale Structure, ed. J. M. Dickey, 175
- Murata, R., Oguri, M., Nishimichi, T., et al. 2019, *PASJ*, **71**, 107
- Nelson, D., Springel, V., Pillepich, A., et al. 2019, *Computational Astrophysics and Cosmology*, **6**, 2
- Oguri, M. 2014, *MNRAS*, **444**, 147
- Old, L., Wojtak, R., Mamon, G. A., et al. 2015, *MNRAS*, **449**, 1897
- Oogi, T., Ishiyama, T., Prada, F., et al. 2022, arXiv e-prints, arXiv:2207.14689
- Pereira, M. E. S., Soares-Santos, M., Makler, M., et al. 2018, *MNRAS*, **474**, 1361
- Pillepich, A., Springel, V., Nelson, D., et al. 2018, *MNRAS*, **473**, 4077
- Pisani, A. 1996, *MNRAS*, **278**, 697
- Planck Collaboration, Ade, P. A. R., Aghanim, N., et al. 2014, *A&A*, **571**, A1
- . 2016, *A&A*, **594**, A13
- Planck Collaboration, Aghanim, N., Akrami, Y., et al. 2018, arXiv e-prints, arXiv:1807.06209
- Pratt, G. W., Croston, J. H., Arnaud, M., & Böhringer, H. 2009, *A&A*, **498**, 361
- Press, W. H., & Schechter, P. 1974, *ApJ*, **187**, 425
- Rozo, E., Wechsler, R. H., Rykoff, E. S., et al. 2010, *ApJ*, **708**, 645
- Rykoff, E. S., Rozo, E., Busha, M. T., et al. 2014, *ApJ*, **785**, 104
- Rykoff, E. S., Rozo, E., Hollowood, D., et al. 2016, *ApJS*, **224**, 1
- Sarazin, C. L. 1988, X-ray emission from clusters of galaxies
- Saro, A., Bocquet, S., Rozo, E., et al. 2015, *MNRAS*, **454**, 2305
- Serra, A. L., Diaferio, A., Murante, G., & Borgani, S. 2011, *MNRAS*, **412**, 800
- Shirasaki, M., Ishiyama, T., & Ando, S. 2021, *ApJ*, **922**, 89
- Simet, M., McClintock, T., Mandelbaum, R., et al. 2017, *MNRAS*, **466**, 3103
- Simet, M., Kubo, J. M., Dodelson, S., et al. 2012, *ApJ*, **748**, 128
- Springel, V. 2010, *MNRAS*, **401**, 791
- Takada, M., Ellis, R. S., Chiba, M., et al. 2014, *PASJ*, **66**, R1
- Tempel, E., Tamm, A., Gramann, M., et al. 2014, *A&A*, **566**, A1
- The, L. S., & White, S. D. M. 1986, *AJ*, **92**, 1248
- Tinker, J., Kravtsov, A. V., Klypin, A., et al. 2008, *ApJ*, **688**, 709
- Tinker, J. L., & Wetzell, A. R. 2010, *ApJ*, **719**, 88
- Tonry, J. L., & Davis, M. 1981, *ApJ*, **246**, 680
- Vikhlinin, A., Burenin, R. A., Ebeling, H., et al. 2009, *ApJ*, **692**, 1033
- Wang, L., & Steinhardt, P. J. 1998, *ApJ*, **508**, 483
- Weinberg, D. H., Mortonson, M. J., Eisenstein, D. J., et al. 2013, *Phys. Rep.*, **530**, 87
- Weinberger, R., Springel, V., & Pakmor, R. 2020, *ApJS*, **248**, 32
- Wen, Z. L., Han, J. L., & Liu, F. S. 2010, *MNRAS*, **407**, 533
- White, S. D. M., & Frenk, C. S. 1991, *ApJ*, **379**, 52
- Wiesner, M. P., Lin, H., & Soares-Santos, M. 2015, *MNRAS*, **452**, 701
- Wilson, G., Cole, S., & Frenk, C. S. 1996, *MNRAS*, **280**, 199
- Yang, X., Mo, H. J., van den Bosch, F. C., et al. 2007, *ApJ*, **671**, 153
- Yee, H. K. C., & Ellingson, E. 2003, *ApJ*, **585**, 215
- Zhang, Y., Jeltrema, T., Hollowood, D. L., et al. 2019, arXiv e-prints, arXiv:1901.07119